Environ Geochem Health
https://doi.org/10.1007/s10653-022-01350-5

ORIGINAL PAPER

Environmental impacts of ^{222}Rn, Hg and CO_2 emissions from the fault zones in the western margin of the Ordos block, China

Zhaofei Liu · Ying Li · Zhi Chen · Zhidan Zhao · Ruilin Huangfu · Yuanxin Zhao · Lei Lei · Chang Lu

Received: 29 July 2021 / Accepted: 9 July 2022

Abstract Investigating the emissions of soil gas including radon, mercury and carbon dioxide (^{222}Rn, Hg and CO_2) from the solid earth to the atmosphere through active fault zones is of great significance for accession of atmospheric environment. In this study, the concentrations and fluxes of ^{222}Rn, Hg and CO_2 were measured at the main active fault zones at the western margin of the Ordos block, China. The concentrations of ^{222}Rn, Hg and CO_2 were in the range of 0–60.1 kBq m^{-3}, 3–81 ng m^{-3} and 0.04–9.23%, respectively, while the fluxes of ^{222}Rn, Hg and CO_2 are in the range of 1.99–306.99 mBq m^{-2} s^{-1}, 0–15.12 ng m^{-2} h^{-1} and 0–37.91 g $m^{-2}d^{-1}$, respectively. Most of the major fault zones at the study area are CO_2 risk-free regions (CO_2 concentration in soil gas < 5%). However, the extend of ^{222}Rn pollution at the fault zones of F_1, F_4, F_5 and F_9 (the fault number) and that of Hg pollution at the fault zones of F_2, F_4, F_5 and F_7 were higher than the pollution level of 1. The annual emission of Hg and CO_2 from the western margin of the Ordos block was estimated to be 2.03 kg and 0.70 Mt, respectively. Comprehensive analyses indicated that the higher emission rates of soil gases from the active fault zones were related to the seismic activities. The results suggest that the earthquake activity is a dominant factor enhancing the emission of ^{222}Rn, Hg and CO_2 from the solid earth through active fault zones and, furthermore, resulting great impact on the atmospheric environment.

Z. Liu · Z. Zhao · R. Huangfu
School of Earth Sciences and Resources, China University of Geosciences, Beijing 100083, China
e-mail: liuzhaofei0@163.com

Z. Zhao
e-mail: zdzhao@cugb.edu.cn

R. Huangfu
e-mail: 2101170183@cugb.edu.cn

Z. Liu · Y. Li · Z. Chen (✉) · Y. Zhao · C. Lu
CEA Key Laboratory of Earthquake Prediction (Institute of Earthquake Forecasting), China Earthquake Administration, Beijing 100036, China
e-mail: dugu_830822@163.com

Y. Li
e-mail: subduction6@hotmail.com

Y. Zhao
e-mail: zhaoyuanxin18@ucas.edu.com

C. Lu
e-mail: cealuchang@163.com

L. Lei
China Earthquake Networks Center, Beijing 100045, China
e-mail: leilei@seis.ac.cn

C. Lu
Institute of Geophysics, China Earthquake Administration, Beijing 100081, China

Published online: 16 August 2022

Keywords Environmental impact · Soil gas · Earthquake · Active fault zone · Ordos block

Introduction

Radon, mercury and carbon dioxide (^{222}Rn, Hg and CO_2) emissions from the solid earth to the atmosphere can cause great environmental risks (Bem et al., 2021; Cinelli et al., 2015; Gray et al., 2015; Italiano et al., 2009). Emissions of soil gas from the solid earth occur continuously at low levels in most parts of the world, while emissions in some tectonic zones, such as mid-oceanic ridges, volcanoes and active fault zones, are very strong, which severely affects the atmospheric environment (Caracausi et al., 2015; Chavrit et al., 2014; Chiodini et al., 2010; Ciotoli et al., 2007; Phuong et al., 2012; Wang et al., 2018). The fractures in fault zones are the preferential passage for gas migration from the deep crust to the surface because of the much higher permeability and porosity of the fractured rocks relative to the surrounding ones (Chen et al., 2018; Doăn et al., 2009; Fu et al., 2017; Italiano et al., 2013; Ring et al., 2016; Rizzo et al., 2019; Yıldırım et al., 2020). Therefore, amounts of investigations of emissions from the active faults by measuring soil gases were conducted recently throughout the world, *e.g.,* in China, the Americas, Turkey, Italy, etc. (Doăn et al., 2009; Jung et al., 2015; Kulongoski et al., 2013; Lewicki et al., 2013; Yuce et al., 2014, 2017; Zhou et al., 2016). A large amount of soil gas emitted to the atmosphere were frequently observed at active fault zones (Chiodini et al., 2010; Han et al., 2014; Italiano et al., 2014; Jung et al., 2014; Kámpf et al. 2013; Tao et al., 2005).

Elevated CO_2 concentrations affect the respiratory systems of humans and other animals, even causing hypoxia and suffocation in the worst cases (Chiodini et al., 2010). ^{222}Rn is a colorless, odorless and radioactive inert gas produced by the decay of natural uranium (^{238}U). ^{222}Rn has a half-life of 3.8 days, and it exists prevalently in the solid earth's crust. The atmospheric ^{222}Rn may enter the lungs through inhalation and radiate lung tissues (Bajwa et al., 2003; Harrison, 2003). As a result, ^{222}Rn has been identified as the second highest cause of lung cancer after smoking (Lubin et al., 2004; Park et al., 2008; Yuce & Gasparon, 2013). Active fault zones, which have developed various fissures and thus have relatively high permeability, are important passages for the emissions of soil gas from the deep part of the solid earth (Capaccioni et al., 2015; Gold, 1979; Zheng et al., 2013, 2017). Carried by gas (CO_2, N_2, etc.), ^{222}Rn existing in the earth's interior continuously migrates to the surface through active fault zones by diffusion and advection (Ciotoli et al., 2007). The main source of Hg in the global atmosphere is Hg in the solid earth (Bajwa et al., 2003; Lindqvist et al., 1991). Hg is stable in liquid form at ambient condition, but it can be easily volatilized into highly toxic Hg vapor when heated. Inhalation of large amounts of Hg vapor can lead to acute Hg poisoning, causing diseases like hepatitis, nephritis, proteinuria, hematuria, and uremia (Tennant 1961). The CO_2 emissions of Mefite d'Ansanto event in Italy caused many fatalities of people and animals (Chiodini et al., 2010; Pfanz et al., 2019). The ^{222}Rn emitted from the fault zones in the Bohai Bay basin in eastern China reached the pollution level of 2–4 according to the Chinese code, which is at high environmental risk and relative prevention measures should be taken (Chen et al., 2018). The maximum fluxes of ^{222}Rn, Hg and CO_2 emitted from soil at the co-seismic rupture zones produced by the Wenchuan M_S 8.0 earthquake were 580.4 mBq m^{-2} s^{-1}, 387.7 ng m^{-2} h^{-1} and 259.2 g $m^{-2}d^{-1}$, respectively, and the total amounts of Hg and CO_2 emissions were estimated to be 15.94 kg yr^{-1} and 0.95 Mt yr^{-1} (Zhou et al., 2017). Therefore, it is necessary to investigate the emissions of ^{222}Rn, Hg and CO_2 from active fault zones and assess environmental risks as part of land-use planning (Chen et al., 2018).

The Ordos block, which is located in the middle of China, has abundant natural resources of gas, oil, coal and uranium (He et al., 2009). There are numerous active faults around the block (SSB 1988). As reported, 91 earthquakes of magnitude larger than 5.0 have occurred in the western margin of the Ordos block since AD 406 (Gao et al., 2016; Liu et al., 2016; Wesnousky et al., 1984), which may enhance the emissions of ^{222}Rn, Hg and CO_2 from the fault zones. Cui et al. (2019) studied the spatial variation of surface CH_4 and CO_2 in the western margin of the Ordos block using satellite hyperspectral data. The concentrations of CH_4 and CO_2 were 1905–2472 ppb and 397.5–458.5 ppm, respectively. On the other hand, the concentration distribution of CH_4 and CO_2 from underground is mainly influenced by gas source, passage and stress. Local tectonic environment and stress state change the driving effect of degassing migration. In this paper, soil gas measurements of ^{222}Rn, Hg and CO_2 from various fault zones in the northwest margin of Ordos block are carried out, and the effects of gas emission from active fault zones on the environment are evaluated. This paper aims at assessing the environmental impacts of gas emission from active fault zones by conducting the investigation of concentrations and fluxes of ^{222}Rn, Hg and CO_2 in the western margin of the Ordos block.

Geological setting

The Ordos block is located at the western part of North China Craton, which has experienced deformation due to a dynamic process of geotectonic since the Mesozoic (Zhang et al., 2011). The western margin of the Ordos block is a strip shaped tectonic belt, which is located at the junction of the Ordos block, the Alxa block and the northeastern block of the Qinghai-Tibet block, forming a transition zone between the stable blocks and active zones (Li & Li, 2008). During the Indosinian, Yanshan and Himalayan tectonic movements, due to tectonic extrusion and extension in different directions, the structural systems of a basin-range landscape and fold-thrust belts are developed from west to east. Eleven active faults in the region with different strikes of WN, NS, NE and WE were selected as areas of interest. Six of them (F_5, F_7, F_8, F_9, F_{10} and F_{11}) are normal faults that stretch to the northern part of the study area, and the other five strike-slip faults (F_1, F_2, F_3, F_4 and F_6) occur at the southern part (Fig. 1; Cao, 2001).

In the western margin of the Ordos block, the Paleozoic strata are developed except for the Silurian and Devonian systems, and the Mesozoic-Cenozoic terrestrial sedimentary strata were well developed, with a total thickness of more than 5000 m. Ultra-basic, basic, neutral, acidic and alkaline rocks are widely distributed in the Alxa block. In addition, abundant mineral resources including natural gas and oil, coal and uranium have been found in the Late Paleozoic and Mesozoic-Cenozoic strata (Fig. 1).

Methods

The concentrations and fluxes of ^{222}Rn, Hg and CO_2 were measured in the field along 16 profiles approximately perpendicular to the 11 selected faults. The soil gas survey was carried out during a period of stable weather in August 2017. The measurements were conducted along one or two parallel survey lines at each profile, and the distance between two neighboring survey lines was 10 m. The sampling interval near the fault scarps was 10 m and gradually increased to a maximum of 40 m near the ends of the survey lines. Gas concentrations were measured at locations along the profiles across the fracture zones. The total numbers of concentration measurements for each line ranged from 14 to 16, and gas fluxes were measured at four profiles on each line (Fig. 2).

The RAD7 radon detector, with detection limit of ^{222}Rn which is 3.7 Bq m^{-3}, was used for measuring ^{222}Rn. The GXH-3010-E CO_2 detector, with detection limit of 0.01%, was used for measuring CO_2. The Zeeman effect Hg detector (RA-915+), with detection limit of 1 ng m^{-3}, was used for measuring Hg. The errors of ^{222}Rn, Hg and CO_2 measurements were ±5%, ±3% and ±2%, respectively. The errors between detectors of the same model for measuring ^{222}Rn, Hg and CO_2 are ±5%, ±3% and ±2%, respectively.

The samples of soil gas were collected with a stainless-steel sampling tube of 3 cm outer diameter that was inserted into the ground to a depth of 0.8 m (Chen et al., 2018; Li et al., 2018; Zhou et al., 2010). The stainless-steel sampling tubes were connected with silicon tubes to a detector. The measurements were made continuously sucking the gas from the soil, taking each one after the other. ^{222}Rn concentration was measured 15 min after sampling (the time necessary for ^{218}Po and ^{222}Rn nuclei to reach equilibrium after radioactive decay, which is about five times the half-life of ^{218}Po). In addition, an inlet filter and molecular sieve were used to protect the detector from dust and soil moisture.

Soil gas flux measured by means of the static closed chamber method. The inverted accumulation hemispherical chamber has a volume of 1.68×10^{-2} m^3 and radius of 0.2 m. The gas circulated from the chamber into the instrument and then back into the chamber via a plastic tube (3 mm inner diameter). The variations of gas concentrations inside the chamber during flux measurements were recorded with the instruments (Chen et al., 2019). Soil gas flux was calculated using

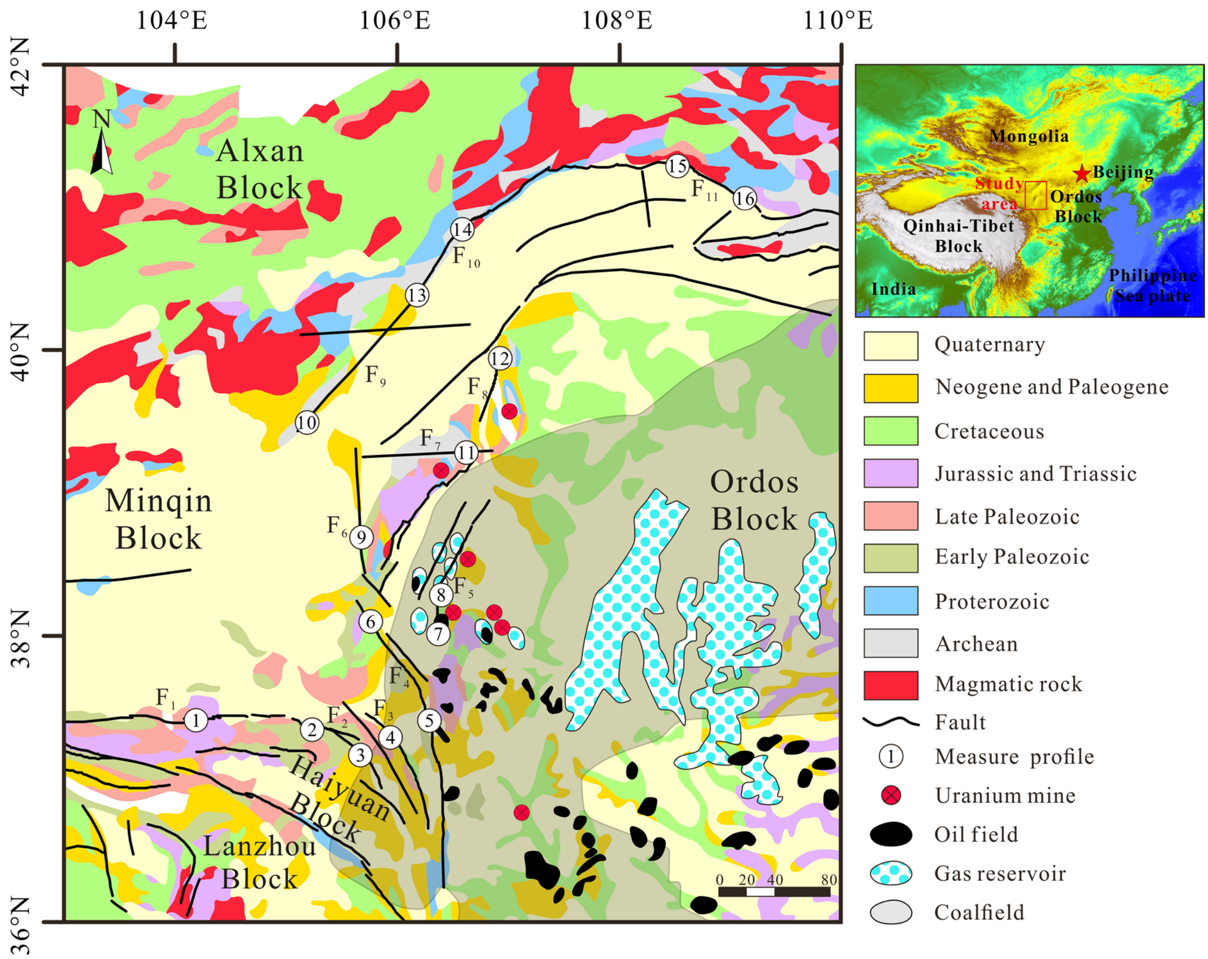

Fig. 1 Schematic geological map of the research region (Liu, 2020). Inset map showed location of the study area in China. F_1: Guanguanling fault; F_2: Xiangshan-Tianjingshan fault; F_3: Yantongshan fault; F_4: Luoshan-Niushoushan fault; F_5: Yellow River fault; F_6: Helanshan West-piedmont fault; F_7: Helanshan East-piedmont fault; F_8: Zhuozishan West-piedmont fault; F_9: Bayanwulashan frontal fault; F_{10}: Langshan frontal fault; F_{11}: Sertengshan frontal fault

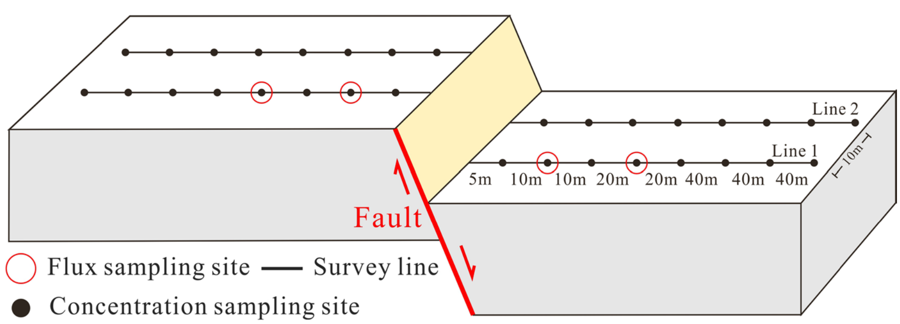

Fig. 2 Sketch of the measuring profile arrangement

the following equation (Chen et al., 2018; Evans et al., 2001; Gerlach et al., 2001):

$$Flux_{gas} = \frac{\Delta C}{A \Delta t} = \frac{V_i P_i T_S}{P_S T_i A} \cdot \frac{dc}{dt} \tag{1}$$

where $Flux_{gas}$ is the soil gas flux, V_i (m^3) and A (m^2) are the volume and bottom region of the chamber, respectively, ΔC is the variation of soil gas concentration with time in the chamber during measuring period Δt (min), P_S and T_S are the standard barometric pressure and temperature, and P_i and T_i are the gas pressure and temperature inside the chamber. The units for $Flux_{Rn}$, $Flux_{Hg}$ and $Flux_{CO2}$ are mBq m^{-2} s^{-1}, ng m^{-2} h^{-1} and g $m^{-2}d^{-1}$, respectively.

Results

The concentrations and fluxes (i.e., minimum, maximum and mean values) of ^{222}Rn, Hg and CO_2 in soil gas from active fault zones at the study area are shown in Tables 1 and 2.

The minimum and maximum concentrations of ^{222}Rn in soil gas at the different profiles ranged from less than the detecting limit to 6.5 kBq m^{-3} and 3.8 to 60.1 kBq m^{-3}, respectively. The mean concentrations of ^{222}Rn at the different profiles were 2.1 to 14.8 kBq m^{-3} (Table 1). The minimum and maximum fluxes of ^{222}Rn ranged from 1.99 to 76.73 mBq m^{-2} s^{-1} and 8.49 to 306.99 mBq m^{-2} s^{-1}, respectively. The mean fluxes of ^{222}Rn ranged from 5.17 to 131.47 mBq m^{-2} s^{-1} (Table 2).

The minimum and maximum concentrations of Hg in soil gas ranged from 3 to 7 ng m^{-3} and 9 to 81 ng m^{-3}, respectively. The mean concentrations of Hg were 8 to 20 ng m^{-3} (Table 1). The minimum and maximum fluxes of Hg ranged from less than the detecting limit to 1.05 ng m^{-2} h^{-1} and less than the detecting limit to 15.12 ng m^{-2} h^{-1}, respectively. The mean flux of Hg ranged from less than the detecting limit to 7.46 ng m^{-2} h^{-1} (Table 2).

The minimum and maximum concentrations of CO_2 in soil gas at the different profiles ranged from 0.04% to 0.38% and 0.08% to 9.23%, respectively (Table 1). The mean concentrations of CO_2 ranged from 0.07% to 2.20%. The minimum and maximum fluxes of CO_2 ranged from 0 to 23.25 g $m^{-2}d^{-1}$ and 5.30 to 37.91 g $m^{-2}d^{-1}$, respectively. The mean flux of CO_2 ranged from 3.72 to 32.18 g $m^{-2}d^{-1}$ (Table 2).

Table 1 Recorded concentrations of ^{222}Rn, Hg and CO_2 in soil gas from active fault zones at the western margin of Ordos block, China

Profile (No.)	Total measuring points	Fault (No.)	^{222}Rn (kBq m^{-3})				Hg (ng m^{-3})				CO_2 (%)			
			Mean	σ	Max	Min	Mean	σ	Max	Min	Mean	σ	Max	Min
1	28	F_1	10.0	5.5	23.7	3.4	11	3	18	6	0.09	0.03	0.14	0.05
2	32	F_2	5.8	1.8	10.0	2.6	15	11	55	7	0.07	0.01	0.08	0.05
3	28		7.0	2.7	13.2	0.0	10	4	19	5	0.14	0.04	0.19	0.08
4	32	F_3	4.9	1.1	7.8	2.3	16	7	34	6	0.08	0.02	0.11	0.04
5	30	F_4	13.2	8.9	40.9	4.4	11	4	22	4	0.09	0.02	0.12	0.07
6	32		5.5	2.9	17.9	2.7	18	11	44	3	0.12	0.02	0.16	0.07
7	32	F_5	10.9	4.3	21.9	6.0	20	17	81	5	2.20	1.68	9.23	0.38
8	32		14.8	7.7	36.7	6.5	12	8	44	4	0.83	0.45	2.02	0.13
9	16	F_6	8.1	9.6	14.8	4.4	8	10	9	5	0.16	0.54	0.24	0.09
10	32	F_9	13.4	14.2	60.1	3.3	11	5	30	6	0.09	0.04	0.18	0.04
11	30	F_7	7.2	2.2	10.8	3.8	10	2	15	6	0.23	0.06	0.36	0.10
12	32	F_8	2.5	1.0	5.0	0.7	12	3	24	7	0.10	0.03	0.23	0.06
13	30	F_{10}	2.1	0.6	3.8	0.7	10	3	16	6	0.13	0.04	0.28	0.07
14	16		9.4	4.2	13.4	1.7	10	4	18	4	0.22	0.09	0.38	0.14
15	30	F_{11}	4.0	1.2	6.2	1.8	9	2	14	4	0.14	0.06	0.44	0.08
16	30		4.4	1.0	6.9	2.6	9	2	13	6	0.11	0.03	0.23	0.07

σ: Standard deviation

Table 2 Recorded fluxes of ^{222}Rn, Hg and CO_2 in soil gas from active fault zones at the western margin of Ordos block, China

Profile (No.)	Total measuring points	Fault (No.)	^{222}Rn (mBq m^{-2} s^{-1})				Hg (ng m^{-2} h^{-1})				CO_2 (g $m^{-2}d^{-1}$)			
			Mean	σ	Max	Min	Mean	σ	Max	Min	Mean	σ	Max	Min
1	4	F_1	109.24	36.20	146.03	76.73	0.68	0.69	1.35	0.00	9.81	7.45	20.38	4.44
2	4	F_2	55.69	18.10	82.56	43.06	0.00	0.00	0.00	0.00	3.72	2.01	5.30	1.02
3	4		28.69	3.25	33.42	26.12	0.17	0.20	0.39	0.00	9.89	4.99	16.36	4.19
4	4	F_3	28.65	11.89	43.85	16.73	0.02	0.04	0.08	0.00	6.46	6.70	16.11	0.95
5	4	F_4	131.47	118.88	306.99	43.25	1.04	0.96	2.33	0.19	9.40	1.33	10.84	7.84
6	4		26.49	10.24	40.50	15.88	2.58	1.04	3.34	1.05	9.44	4.32	13.35	3.28
7	4	F_5	25.73	14.03	45.63	14.00	0.51	0.49	1.22	0.19	32.18	6.42	37.91	23.25
8	4		15.42	10.44	24.50	5.76	2.08	3.44	7.22	0.00	18.13	7.63	26.50	8.59
9	4	F_6	28.31	16.57	49.67	10.83	0.27	0.28	0.52	0.00	13.10	5.24	17.85	6.78
10	4	F_9	39.07	24.14	68.95	12.16	7.46	6.19	15.12	0.97	11.76	7.99	23.66	6.57
11	4	F_7	12.71	7.38	18.24	2.32	0.00	0.00	0.00	0.00	15.17	7.99	23.91	7.10
12	4	F_8	22.82	13.24	37.26	9.12	0.00	0.00	0.00	0.00	10.52	2.83	14.15	7.23
13	4	F_{10}	5.17	2.80	8.49	1.99	0.62	1.25	2.49	0.00	6.54	1.29	7.75	4.79
14	4		17.25	9.80	29.28	7.88	3.69	5.99	12.53	0.00	9.38	10.20	19.72	0.00
15	4	F_{11}	19.60	10.61	33.90	9.26	0.02	0.05	0.10	0.00	12.55	2.55	15.81	9.91
16	4		23.38	8.30	35.60	17.31	0.27	0.31	0.70	0.00	9.71	5.32	16.10	3.67

σ: Standard deviation

Discussion

Emissions of the soil gases from the fault zone

^{222}Rn emissions

It is reported that the ^{222}Rn concentrations from active fault zones were high, ranging from 20 to 80 kBq m^{-3} (Bonforte et al., 2013; Wang et al., 2014; Yang et al., 2018). The mean values of ^{222}Rn concentrations at each measurement profile at the study area were 2.7–14.8 kBq m^{-3}, which were lower than 20 kBq m^{-3}, showing relatively low levels at the 11 active faults. However, the maximum concentrations were much higher at 5 profiles at the southwestern part of the study area, with the highest value of 60.1 kBq m^{-3} measured at the profile No.10, and values of 20~50 kBq m^{-3} at the profiles No.1, 5, 7 and 8. The average fluxes of ^{222}Rn at the profiles No.1, No.2 and No.5 at the southern part were pretty high, with the highest value of 131.5 mBq m^{-2} s^{-1} (Fig. 3b). At the southern part of the study area, the higher values exceeding 50 mBq m^{-2} s^{-1} were obtained at 3 profiles (No.1, 2, 5), with a highest value of 306.99 mBq m^{-2} s^{-1} at the profile No.5.

Based on the method of geoaccumulation index, pollution of ^{222}Rn at the region was analyzed by means of the concentration and flux and the values of maximum emissions from active fault zones. This method avoids natural factors that may cause the background value to change, and neither need to measure other parameters. The formula is as follows (Muller, 1969):

$$I_{geo} = \log_2\left[\frac{C}{1.5 \cdot C_B}\right] \tag{2}$$

where I_{geo} is geoaccumulation index; C is the sample concentration; and C_B is the background concentration. The pollution levels are classified by the I_{geo} index (Table 3). The ^{222}Rn and Hg concentration data in soil gas were adjusted as log-normal distribution by means of a distribution test, and the background values were represented by their geometric means.

Combined with Table 3, Fig. 3a shows that the ^{222}Rn pollution at measuring profiles No.10 (F_9) reached level 3. The ^{222}Rn pollution at measuring profiles No.1 (F_1), No.5 (F_4) and No.8 (F_5) reached level 2. The ^{222}Rn pollution at measuring profiles No.3 (F_2), No.6 (F_4), No.7 (F_5), No.9 (F_6) and No.14 (F_{10}) reached level 1. From the above results, corresponding anti-^{222}Rn measures should be undertaken

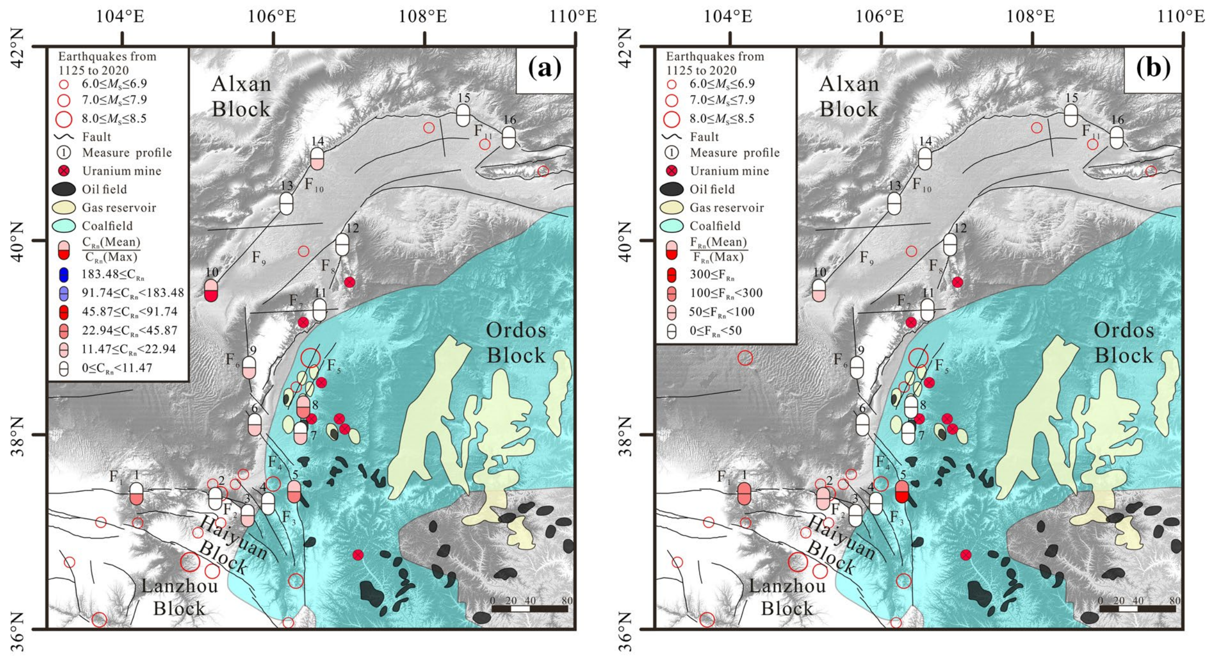

Fig. 3 Distribution maps of ^{222}Rn concentrations (C_{Rn}) and fluxes (F_{Rn}) at active faults in the western margin of the Ordos block **a**–**b** represents the average concentration, maximum concentration, average flux and maximum flux of ^{222}Rn component measured). Earthquake events extracted from https://data.earthquake.cn/gcywfl/index.html

Table 3 Geoaccumulation index in relation to pollution extent (Muller, 1969)

Pollution level	I_{geo}	Pollution intensity
0	$I_{geo} \leq 0$	Unpolluted
1	$0 < I_{geo} \leq 1$	Unpolluted to moderately polluted
2	$1 < I_{geo} \leq 2$	Moderately to strongly polluted
3	$2 < I_{geo} \leq 3$	Strongly polluted
4	$3 < I_{geo} \leq 4$	Strongly to very strongly polluted
5	$4 < I_{geo}$	Very strongly polluted

for those areas in the fault zone according to the pollution levels.

Hg emissions

The Hg concentrations in soil gas at the study area ranged from 3 to 81 ng m^{-3}, with a mean value of 12 ng m^{-3} (Fig. 4a), which is much higher than the concentration of background atmospheric Hg in the northern hemisphere (Li et al., 2014; 1.5 ~ 2.0 ng m^{-3}). The max value of Hg flux was 15.12 ng m^{-2} h^{-1} (132 g km^{-2} yr^{-1}), which is higher than the global Hg flux (from natural sources), with a mean value of 6 g km^{-2} yr^{-1} (Lindqvist et al., 1991), and close to the max value of Hg flux (18.7 ng m^{-2} h^{-1}) from the rupture zone produced by the Wenchuan M_S 8.0 earthquake (Zhou et al., 2016). The higher Hg flux mainly occurs on the F_4, F_5, F_9 and F_{10} (Fig. 4b).

Based on the Hg concentration in soil gas, Hg pollution was quantitatively evaluated using the geoaccumulation index method, as expressed by formula (2) (Muller, 1969). Especially most half of the region reached the I_{geo} level 1 to 2, and only one reached the level 3, indicating that Hg protection and prevention should be strengthened for this region. Figure 4a shows that the Hg pollution at measuring profiles No.7 (F_5) reached level 3. The Hg pollution at measuring profiles No.2 (F_2), No.6 (F_4), No.8 (F_5) and No.11 (F_7) reached level 2. The Hg pollution at measuring profiles No.3 (F_2), No.4 (F_3), No.5 (F_4), No.10 (F_9) and No.12 (F_8) reached level 1.

The total amounts of emitted gases from the fault zones at the study area were estimated in order to evaluate the impact of the gases on the local atmospheric environment. The total amount of emitted

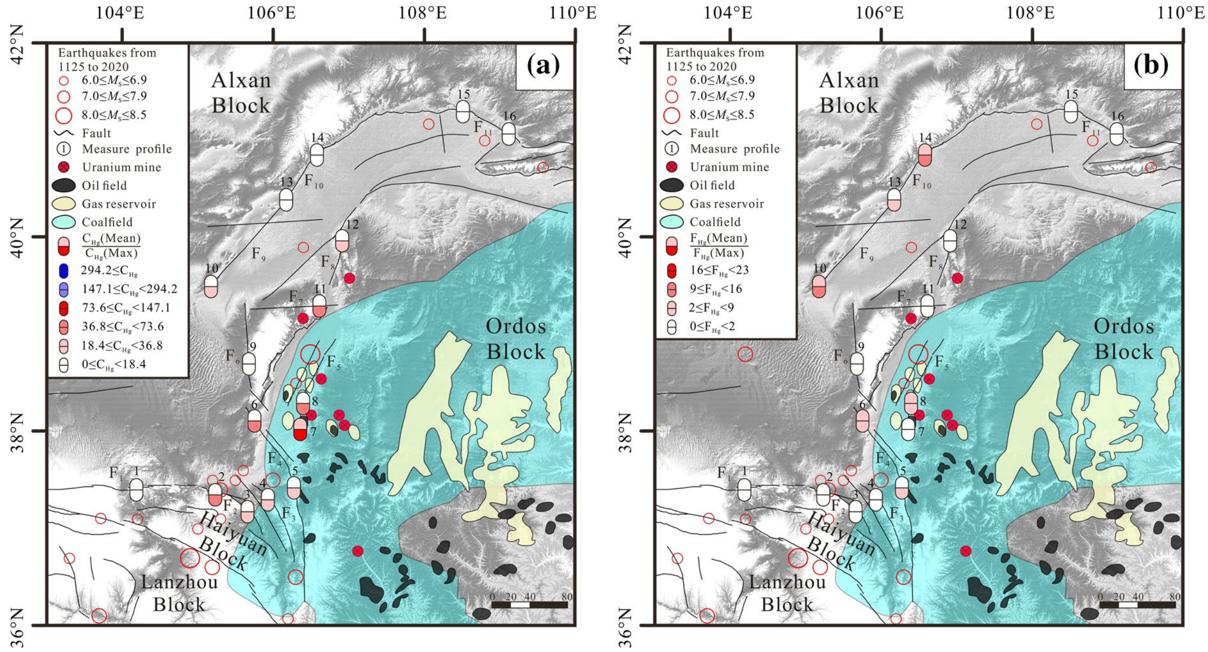

Fig. 4 Distribution maps of Hg concentrations (C_{Hg}) and fluxes (F_{Hg}) in active faults in the western margin of the Ordos block (**a**–**b** represents the average concentration, maximum concentration, average flux and maximum flux of Hg component measured). Earthquake events extracted from https://data.earthquake.cn/gcywfl/index.html

gases is a function of the fluxes of soil gases at the region of active faults. The annual output of a gaseous component was calculated using the equation:

$$C_{\text{gas}} = \overline{F}_{\text{gas}} \times S \times 24h \times 365d \quad (3)$$

where C_{gas} is the annual output of a gas component to the atmosphere; $\overline{F}_{\text{gas}}$ is the flux of gas component; and S is the area (which equals length by width, in m^2) of each fault zone, which equals length by width of each fault zones. For Hg, $\overline{F}_{\text{Hg}}$ unit is ng m^{-2} h^{-1}.

It was estimated that about 5207 t from Hg of global natural sources is emitted annually to the atmosphere (Pirrone et al., 2010). The annual contribution of Hg in soil gas from the western margin of the Ordos block to the atmosphere was calculated as 2.03 kg, which is much higher than the values from the Xiadian active fault zone (1.3 kg yr^{-1}; Li et al., 2018) and the Wenchuan earthquake rupture zone (0.688 kg yr^{-1}; Zhou et al., 2016).

CO_2 emissions

The mean concentrations of CO_2 were in the range of 0.07–2.20% from the main active fault zone of the western margin of the Ordos block. The maximum concentration of the two measurement profiles on fault F_5 reached 2.20% and 0.83%, which is much higher than the others (Fig. 5a). However, lush vegetation covers these two regions. Few vegetations exist near other profiles and even some of them are Gobi beaches where they have no vegetation distribution around. Therefore, the higher CO_2 concentrations in the two regions could be attributed to the vegetation respiration. CO_2 flux is mainly higher in No.1, No.7, No.8, No.10, No.11 and No.14, and the highest flux also occurs on F_5 (Fig. 5b).

The classification of hazard levels from Baxter et al. (1999) was used to get the risk levels of CO_2 in soil gas at 70 cm. When the concentration of CO_2 in soil gas is below 1.5%, the danger level is 1, stating for no hazard at any time, which is equivalent to the concentration of carbon dioxide at non-volcanic regions. When the concentration of CO_2 range is 1.5 ~ 5%, the danger level is 2. There is no risk

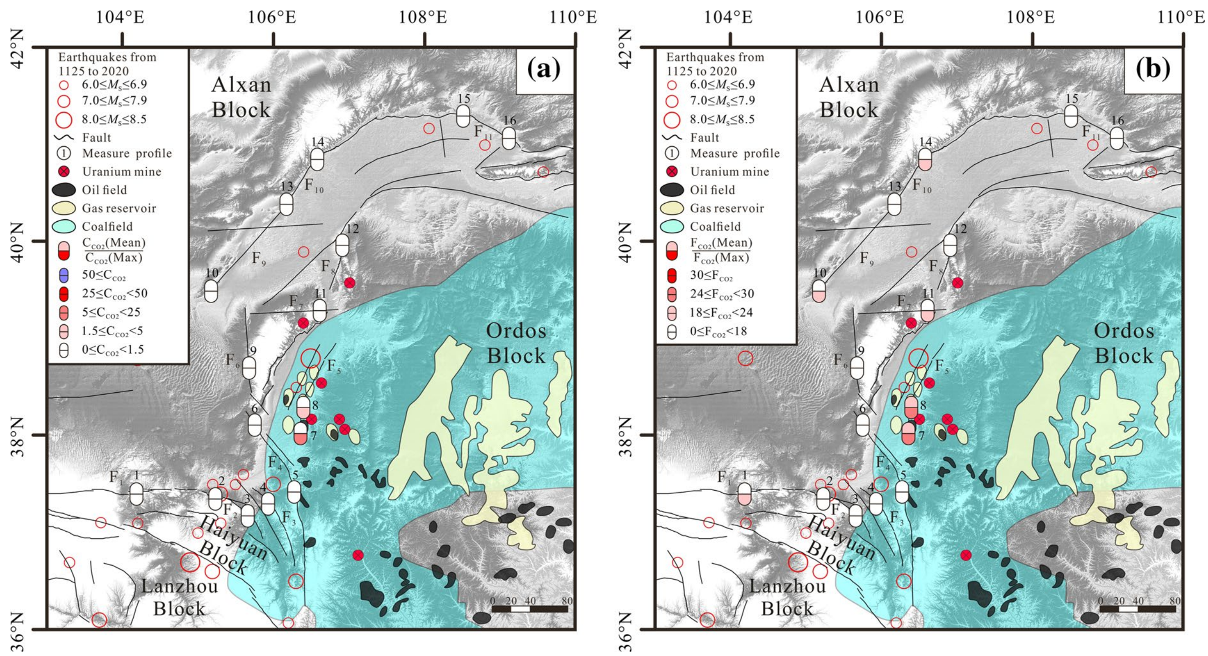

Fig. 5 Distribution maps of CO_2 concentrations (C_{CO2}) and fluxes (F_{CO2}) in active faults in the western margin of the Ordos block (**a**–**b** represents the average concentration, maximum concentration, average flux and maximum flux of CO_2 component measured). Earthquake events extracted from https://data.earthquake.cn/gcywfl/index.html

of asphyxia, which means weak emissions of soil gas and no dangerous activities of CO_2 in houses or spaces below ground. When the concentration of CO_2 range is 5–25%, the danger level is 3. There is a low risk of asphyxia, which will accumulate lethal amounts of CO_2 in spaces below ground, and some evidence of CO_2 contamination at bed level in houses. When the concentration of CO_2 range is 25–50%, the danger level is 4. There is a moderate risk of asphyxia, which means accumulation of CO_2 in spaces below ground and concentration up to 1% CO_2 commonly measured at bed level in houses. When the concentration of CO_2 is beyond 50%, the danger level is 5. There is a high risk of asphyxia, which means lethal concentration of CO_2 within a few hours in all spaces below ground and lethal concentration of CO_2 (15%) found at ground level in the houses. In this study, the maximum CO_2 concentration in soil gas got almost 9.23% at the profiles 7 and 8 in the Yellow River fault zone (F_5 fault). This region can be regarded as a level 3 danger zone, and there is a risk of CO_2 accumulation and death in confined spaces; hence, it should be given attention and corresponding treatment. However, the concentrations of CO_2 at the other measuring profiles in this zone were in the range 0.04–0.44% (Fig. 5), which are considered as risk-free.

The annual output of CO_2 was calculated by using Eq. (3), and the units of F_{CO2} are g $m^{-2}d^{-1}$. The annual contribution of CO_2 from fault zone of the western margin Ordos block was calculated as 1,924 t d^{-1} (0.70 Mt yr^{-1}; Table 4), which is basically same as the Wenchuan earthquake rupture zone (0.95 Mt; Zhou et al., 2017). This is quit below the annual contribution of the Xiadian active fault zone of 2 Mt (Li et al., 2018), which accounts for about 5% of the atmospheric contribution rate of CO_2 from new generation, typical of volcanic geothermal regions in mainland China (Tibet Gulu-Yadong Rift Valley, Changbaishan Tianchi, Wudalian Pool, etc.).

Dominant factors affecting the emissions of soil gas

Generally, the main factors affecting the distribution of soil gas are gas origin, tectonic activity, rock types, vegetation, and meteorological conditions (Fu et al., 2005; Han et al., 2014; Hinkle, 1994; Lehmann et al.,

Table 4 Recorded average flux and output of Hg and CO_2 in active faults in the western margin of the Ordos block

Profile (No.)	Fault	Length (km)	Area ($\times 10^6$ m^2)	Mean $flux_{Hg}$ (ng m^{-2} h^{-1})	Hg output (g d^{-1})	Hg output (g yr^{-1})	Mean $flux_{CO2}$ (g $m^{-2}d^{-1}$)	CO_2 output (t d^{-1})	CO_2 output (t yr^{-1})
1	F_1	60	3	0.68	0.05	18	9.81	29.43	10,742
2	F_2	140	28	0.00	0.06	21	3.72	190.54	69,547
3				0.17			9.89		
4	F_3	110	11	0.02	0.00	2	6.46	71.06	25,937
5	F_4	150	15	1.04	0.65	238	9.40	141.30	51,575
6				2.58			9.44		
7	F_5	130	13	0.51	0.40	147	32.18	327.02	119,360
8				2.08			18.13		
9	F_6	100	10	0.27	0.07	24	13.10	131.00	47,815
10	F_9	100	10	7.46	1.79	654	11.76	117.60	42,924
11	F_7	120	12	0.00	0.00	0	15.17	182.04	66,445
12	F_8	150	15	0.00	0.00	0	10.52	157.80	57,597
13	F_{10}	160	48	0.62	2.48	906	6.54	382.08	139,459
14				3.69			9.38		
15	F_{11}	175	17.5	0.02	0.06	23	12.55	194.78	71,093
16				0.27			9.71		

2000; Lombardi & Voltattorni, 2010; Papp et al., 2008; Toutain & Baubron, 1999; Walia et al., 2009; Winkler et al., 2001; Yuce et al., 2010; Zhou et al., 2010). The measurements were conducted under the same meteorological conditions in the same tectonic background and similar natural environment, so it is reasonable to predict that the gas emission should be dominantly controlled by other potential factors.

The study area is located in the transitional zone between arid and semiarid areas, with a continental climate and low annual rainfall. Most of this region is Gobi and desert with little vegetation. In addition, the field measurements were completed in August, during which there was no rainfall over the entire measurement period, and meteorological conditions were similar across the study area. Therefore, the influences of meteorological condition and surface vegetation on the ^{222}Rn emissions in soil gas at this study area can be ignored.

Due to the destruction of active faults, the concentration of ^{222}Rn in uranium mining regions is particularly high (Fu et al., 2008; Varley & Flowers, 1993). The measuring fault zones F_5, F_7 and F_8 have been identified near several uranium ore deposits (Fig. 1; Jia et al., 1997; Wei & Wang, 2004). However, the mean concentrations and fluxes of ^{222}Rn at these profiles were 36.7 kBq m^{-3} and 45.63 mBq m^{-2} s^{-1}, respectively. But, the highest ^{222}Rn concentration is 60.1 kBq m^{-3}, which appeared on the F_9, and the highest ^{222}Rn flux is 306.99 mBq m^{-2} s^{-1}, which appeared on the F_4. The reason is that uranium ore deposits are deeply buried in this region and that active faults do not cut the uranium ore deposits. As a result, the ^{222}Rn gas produced by uranium ore has not been transported to the surface through faults.

In addition, the emission contents of ^{222}Rn gas released by rocks with different lithology are diverse. Generally, the emission content released by granite is the highest, followed by shale, limestone and sandstone (Baixeras et al., 2001; El-Arabi et al., 2006). As shown in Fig. 1, granite is widely distributed at the northern part of the study area. However, the maximum concentrations and fluxes of ^{222}Rn (0.2–13.4 kBq m^{-3}, 8.5–35.6 mBq m^{-2} s^{-1}) at the measuring profiles No. 13, 14, 15 and 16 at the northern part were much lower than that at the southern part (0.1–9.2 kBq m^{-3}, 18.24–306.99 mBq m^{-2} s^{-1}) of the study area (Fig. 3). It can be concluded that the granite is not be the main contributor to the ^{222}Rn emissions in soil gas at the study area.

Measuring profiles No. 7 and 8 in fault zone F_5 are located in areas which are rich in coal, oil and natural gas (Jia et al., 1997; Wei & Wang, 2004). However, the maximum concentration and CO_2 flux in soil gas at these observation profiles were lower, 9.23% and 37.91 g $m^{-2}d^{-1}$, respectively, than those at the Xiadian, Longmenshan and Tangshan active faults (Chen et al., 2018, 2019; Li et al., 2018; Zhou et al., 2010) (Fig. 5), indicating that coal, oil and natural gas may not be the main sources for CO_2 in soil gas at this study area. Moreover, thermomethamorphic and mechanochemical reactions may also be responsible for the generation of CO_2 (Italiano et al., 2008; Martinelli & Plescia, 2003).

Changes in fracture permeability caused by tectonic activity in the fault zone are the main factors leading to changes the ^{222}Rn and Hg emissions in soil gas. Fissures in the fault zone are the main channels for deep gas migration to the surface (Fu et al., 2008; Li et al., 2013). Previous studies have found that the P-wave velocity structure below the western margin of the Ordos block showed obvious heterogeneity and significant zoning and block characteristics. The 200–300 km depth range of the upper mantle in the southern of the lithosphere showed high-speed anomalies, while the north the upper mantle showed a large area of low-velocity anomalies (Gao et al., 2016). The anomalous velocity structure also indicates that the deformation of the lithosphere at the southern part of the area is mainly squeezed by the arc tectonic belt on the northeastern margin of the Qinghai-Tibet Plateau and forms a foreland basin, while the Yinchuan fault depression basin and Hetao depression basin in the north are stretched stress formation (Cao, 2001; Liu et al., 2019; Wang et al., 2017). Due to the northeast compression of the Qinghai-Tibet Plateau, the low-velocity material in the upper mantle migrated to the bottom of the lithosphere at the northern part of the western margin of Ordos block and continued to surge in the weak position of the lithosphere (ancient suture zone or fissure), which caused the northern lithosphere to thin (Gao et al., 2016; Liu et al., 2016). This leads to significant differences in the thickness of the lithosphere between the southern and northern parts of the western margin of Ordos block. The thickness of the lithosphere in the northern part is about 200 km, while the thickness at the southern part is about 400 km (Wang et al., 2017; Yin & Harrison, 2000). The difference in tectonic activity makes the fracture development degree and fracture permeability in the fault zone very different, and the concentrations and fluxes of deep gas moving near the surface also show corresponding differences. This difference also leads to differences in hydrocarbon generation and mineralization mechanisms and is also reflected in the distribution of mineral resources: large natural gas fields and large coal fields are the main part in the north, and oil fields and medium and small coal fields are the main parts at the southern part.

As is shown in Figs. 3, 4 and 5, the high emissions of ^{222}Rn, Hg and CO_2 from active fault zones are mainly presented at the southern part of the study area. The southern part of the western margin of the Ordos block is an arc-shaped tectonic region in the northeastern corner of the Qinghai-Tibet Plateau (Wang et al., 2017). Under the continuous compression of blocks at the northeastern part of the Indian plate, the region has experienced strong tectonic activity and frequent strong earthquakes since the Quaternary (Table 1; Zhan et al., 2005). Since records began, there have been 23 earthquakes of magnitude 6 or above at the western margin of the Ordos block, eight earthquakes of magnitude 7 or above, and two earthquakes of magnitude 8 or above at the southern part of the western margin of the Ordos block (Gao et al., 2016; Liu et al., 2016; Wesnousky et al., 1984). Previous studies have found that seismic activity is an important factor promoting soil gas emissions from active fault zones in the Ordos block (Chen et al., 2018, 2019; Martinelli, 2020; Zhou et al., 2016). Therefore, the strong legacy seismic activities are predicted to be the dominant influencing factor on the emissions of soil gas including ^{222}Rn, Hg and CO_2 from active fault zones at the southern part of the western margin of the Ordos block.

Conclusions

The field measurements of ^{222}Rn, Hg and CO_2 emissions including concentrations and fluxes from the main active fault zones in the western margin of the Ordos block were conducted. The ^{222}Rn pollution at fault zones F_1, F_4, F_5 and F_9 in the western margin of the Ordos block was not lower than level 1, which suggests that corresponding anti-^{222}Rn measures should be adopted in these areas according to the method of geoaccumulation index. The Hg pollution at fault zones F_2, F_4, F_5 and F_7 was not lower than level 1, which also needs the prevention measures. It is estimated that the annual release of soil gas

Hg from the western margin of the Ordos block is 2.03 kg. Most of the major fault zones at the western margin of the Ordos block are CO_2 risk-free regions (CO_2 concentration in soil gas < 5%). It is estimated that the annual CO_2 emission in soil gas from the western margin of the Ordos block is 0.70 Mt yr^{-1}. It can be concluded that strong seismic activities in this region may be the dominant impact factor causing the high emissions of ^{222}Rn, Hg and CO_2 from the main active fault zones in the western margin of the Ordos block.

Acknowledgements This study was jointly supported by the National Key Research and Development Program of China (No.2019YFC1509203), the Natural Science Foundation of China (Nos. 41402298, 42073063), the Basic Science Research Plan of the Institute of Earthquake Science, China Earthquake Administration (Nos. 2020IEF0704, 2019IEF0303).

Author contributions Z.L. and Z.C. were involved in conceptualization, data analysis and interpretation, manuscript preparation and verification, and review process; Y.L. was involved in methods elaboration and validation, manuscript verification and corrections, and review process; R.H. was involved in experimental works, data analysis and interpretation, and manuscript preparation; and Z.Z. was involved in methods validation and manuscript verification; Y.Z., L.L. and C.L. were involved in investigation, data acquisition, data curation.

Funding The National Key Research and Development Program of China (No.2019YFC1509203), the Natural Science Foundation of China (Nos. 41402298, 42073063), the Basic Science Research Plan of the Institute of Earthquake Science, China Earthquake Administration (Nos. 2020IEF0704, 2019IEF0303).

Data availability The datasets generated and/or analyzed during the current study are available from the corresponding author on reasonable request.

Declarations

Conflict of interest The authors have no financial or proprietary interests in any material discussed in this paper.

Human and animal rights Not applicable since the manuscript has not been involved the use of any animal or human data or tissue.

References

Baixeras, C., Erlandsson, B., Font, L., & Jönsson, G. (2001). Radon emanation from soil samples. *Radiation Measurements, 34*, 441–443. https://doi.org/10.1016/s1350-4487(01)00203-7

Bajwa, B. S., Sharma, N., Walia, V., & Virk, H. S. (2003). Measurements of natural radioactivity in some water and soil samples of Punjab state, India. *Indoor and Built Environment, 12*, 357–361. https://doi.org/10.1177/1420326X03035631

Baxter, P. J., Baubron, J. C., & Coutinho, R. (1999). Health hazards and disaster potential of ground gas emissions at furnas volcano, São Miguel, Azores. *Journal of Volcanology and Geothermal Research, 92*(1), 95–106. https://doi.org/10.1016/S0377-0273(99)00070-0

Bem, H., Długosz-Lisiecka, M., Mazurek-Rudnicka, D., & Szajerski, P. (2021). Occurrence of ^{222}Rn and $^{226,228}Ra$ in underground water and ^{222}Rn in soil and their mutual correlations for underground water supplies in southern Greater Poland. *Environmental Geochemistry and Health, 43*, 3099–3114. https://doi.org/10.1007/s10653-020-00792-z

Bonforte, A., Federico, C., Giammanco, S., Guglielmino, F., Liuzzo, M., & Neri, M. (2013). Soil gases and SAR measurements reveal hidden faults on the sliding flank of Mt. Etna (Italy). *Journal of Volcanology and Geothermal Research, 251*, 27–40. https://doi.org/10.1016/j.jvolgeores.2012.08.010

Cao, G. (2001). *Earthquake research in Inner Mongolia* (pp. 1–174). Beijing: Seismological Press.

Capaccioni, B., Tassi, F., Cremonini, S., Sciarra, A., & Vaselli, O. (2015). Ground heating and methane oxidation processes at shallow depth in Terre Calde di Medolla (Italy): Observations and conceptual model. *Journal of Geophysical Research: Solid Earth, 120*, 3065–3076. https://doi.org/10.1002/2014JB011635

Caracausi, A., Paternoster, M., & Nuccio, P. M. (2015). Mantle CO_2 degassing at Mt. Vulture volcano (Italy): Relationship between CO_2 outgassing of volcanoes and the time of their last eruption. *Earth and Planetary Science Letters, 411*, 268–280. https://doi.org/10.1016/j.epsl.2014.11.049

Chavrit, D., Humler, E., & Grasset, O. (2014). Mapping modern CO_2 fluxes and mantle carbon content all along the mid-ocean ridge system. *Earth and Planetary Science Letters, 387*, 229–239. https://doi.org/10.1016/j.epsl.2013.11.036

Chen, Z., Li, Y., Liu, Z., Wang, J., Zhou, X., & Du, J. (2018). Radon emission from soil gases in the active fault zones in the Capital of China and its environmental effects. *Scientific Reports, 8*(16772), 1–12. https://doi.org/10.1038/s41598-018-35262-1

Chen, Z., Li, Y., Liu, Z., Zheng, G., Xu, W., Yan, W., & Yi, L. (2019). CH_4 and CO_2 emissions from mud volcanoes on the southern margin of the Junggar Basin, NW China: Origin, output, and relation to regional tectonics. *Journal of Geophysical Research: Solid Earth, 124*, 1–15. https://doi.org/10.1029/2018jb016822

Chiodini, G., Granieri, D., Avino, R., Caliro, S., Costa, A., Minopoli, C., & Vilardo, G. (2010). Non-volcanic CO_2 Earth degassing: Case of Mefite d'Ansanto (southern Apennines), Italy. *Geophysical Research Letters, 37*(L11303), 1–4. https://doi.org/10.1029/2010gl042858

Cinelli, G., Tositti, L., Capaccioni, B., Brattich, E., & Mostacci, D. (2015). Soil gas radon assessment and development of a radon risk map in Bolsena, Central Italy. *Environmental Geochemistry and Health, 37*, 305–319. https://doi.org/10.1007/s10653-014-9649-9

Ciotoli, G., Lombardi, S., & Annunziatellis, A. (2007). Geostatistical analysis of soil gas data in a high seismic intermontane basin: Fucino Plain, central Italy. *Journal of Geophysical Research: Solid Earth, 112*(B05407), 1–23. https://doi.org/10.1029/2005JB004044

Cui, Y. J., Li, Y., Si, X. Y., Yang, L. X., Liu, Z. F., Sun, F. X., Li, X. Y., Zheng, H. W., & Du, J. G. (2019). Tectonic controls on near-surface variations in CH_4 and CO_2 concentrations along the northwestern margin of the Ordos Block, China. *Geofluids, 7909483*, 1–10. https://doi.org/10.1155/2019/7909483

Doăn, T., Sumino, H., Nagao, K., Notsu, K., Tuncer, M. K., & Celik, C. (2009). Adjacent releases of mantle helium and soil CO_2 from active faults: Observations from the Marmara region of the North Anatolian Fault zone, Turkey. *Geochemistry, Geophysics, Geosystems, 10*(11), Q11009. https://doi.org/10.1029/2009GC002745

El-Arabi, A. M., Abbady, A., Ahmed, N. K., Michel, R., El-Kamel, A. H., & Abbady, A. G. E. (2006). Assessment of radon-222 concentrations and exhalation rates of rocks and building materials. *Indian Journal of Pure and Applied Physics, 44*(4), 287–291.

Evans, W. C., Sorey, M. L., Kennedy, B. M., Stonestrom, D. A., Rogie, J. D., & Shuster, D. L. (2001). High CO_2 emissions through porous media: Transport mechanisms and implications for flux measurement and fractionation. *Chemical Geology, 177*, 15–29. https://doi.org/10.1016/S0009-2541(00)00379-X

Fu, C. C., Yang, T. F., Du, J., Walia, V., Chen, Y. G., Liu, T. K., & Chen, C. H. (2008). Variations of helium and radon concentrations in soil gases from an active fault zone in southern Taiwan. *Radiation Measurements, 43*, 348–352. https://doi.org/10.1016/j.radmeas.2008.03.035

Fu, C. C., Yang, T. F., Tsai, M. C., Lee, L. C., Liu, T. K., Walia, V., Chen, C. H., Chang, W. Y., Kumar, A., & Lai, T. H. (2017). Exploring the relationship between soil degassing and seismic activity by continuous radon monitoring in the Longitudinal Valley of eastern Taiwan. *Chemical Geology, 469*, 163–175. https://doi.org/10.1016/j.chemgeo.2016.12.042

Fu, C. C., Yang, T. F., Walia, V., & Chen, C. H. (2005). Reconnaissance of soil gas composition over the buried fault and fracture zone in southern Taiwan. *Geochemical Journal, 39*, 427–439. https://doi.org/10.2343/geochemj.39.427

Gao, L., Hou, D., Li, J., Li, S., Dai, Y., Xiong, F., & Yang, H. (2016). Movement characteristics and present seismic activity of Ordos Block. *Geodesy and Geodynamics, 7*(6), 451–458. https://doi.org/10.1016/j.geog.2016.07.008

Gerlach, T. M., Doukas, M. P., Mcgee, K. A., & Kessler, R. (2001). Soil efflux and total emission rates of magmatic CO_2 at the Horseshoe Lake tree kill, Mammoth mountain, California, 1995–1999. *Chemical Geology, 177*, 101–116. https://doi.org/10.1016/S0009-2541(00)00385-5

Gold, T. (1979). Terrestrial sources of carbon and earthquake outgassing. *Journal of Petroleum Geology, 1*(3), 3–19. https://doi.org/10.1111/j.1747-5457.1979.tb00616.x

Gray, J. E., Theodorakos, P. M., Fey, D. L., & Krabbenhoft, D. P. (2015). Mercury concentrations and distribution in soil, water, mine waste leachates, and air in and around mercury mines in the Big Bend region, Texas, USA. *Environmental Geochemistry and Health, 37*, 35–48. https://doi.org/10.1007/s10653-014-9628-1

Han, X., Li, Y., Du, J., Zhou, X., Xie, C., & Zhang, W. (2014). Rn and CO_2 geochemistry of soil gas across the active fault zones in the capital area of China. *Natural Hazards and Earth System Science, 14*(10), 2803–2815. https://doi.org/10.5194/nhess-14-2803-2014

Harrison, J. (2003). Invited editorial: Carcinogenic risk from hot particle exposures-has ICRP got it right? *Journal of Radiological Protection, 23*(1), 1–3. https://doi.org/10.1088/0952-4746/23/1/002

He, D., Li, D., Wu, X., & Wen, Z. (2009). Basic types and structural characteristics of uplifts: An overview of sedimentary basins in China. *Acta Geologica Sinica, 83*(2), 321–346.

Hinkle, M. E. (1994). Environmental conditions affecting concentrations of He, CO_2, O_2 and N_2 in soil-gases. *Applied Geochemistry, 9*(1), 53–63. https://doi.org/10.1016/0883-2927(94)90052-3

Italiano, F., Bonfanti, P., Ditta, M., Petrini, R., & Slejko, F. (2009). Helium and carbon isotopes in the dissolved gases of Friuli Region (NE Italy): Geochemical evidence of CO_2 production and degassing over a seismically active area. *Chemical Geology, 266*(1–2), 76–85. https://doi.org/10.1016/j.chemgeo.2009.05.022

Italiano, F., Martinelli, G., & Plescia, P. (2008). CO_2 degassing over seismic areas: The role of mechanochemical production at the study case of central apennines. *Pure and Applied Geophysics, 165*, 75–94. https://doi.org/10.1007/s00024-007-0291-7

Italiano, F., Sasmaz, A., Yuce, G., & Okan, O. O. (2013). Thermal fluids along the east anatolian fault zone (EAFZ): Geochemical features and relationships with the tectonic setting. *Chemical Geology, 339*, 103–114. https://doi.org/10.1016/j.chemgeo.2012.07.027

Italiano, F., Yuce, G., Uysal, I. T., Gasparon, M., & Morelli, G. (2014). Insights into mantle-type volatiles contribution from the dissolved gases in artesian waters of the Great Artesian Basin, Australia. *Chemical Geology, 378–379*, 75–88. https://doi.org/10.1016/j.chemgeo.2014.04.013

Jia, J. D., He, G. Q., Li, M. S., Zhou, D. H., & Zhang, L. X. (1997). Structural feature of basement in the Ordos basin and its control to Paleozoic gas. *Geological Journal of China Universities, 3*(2), 144–153. (in Chinese with English abstract).

Jung, N. H., Han, W. S., Han, K., & Park, E. (2015). Regional-scale advective, diffusive, and eruptive dynamics of CO_2 and brine leakage through faults and wellbores. *Journal of Geophysical Research: Solid Earth, 120*(5), 3003–3025. https://doi.org/10.1002/2014JB011722

Jung, N. H., Han, W. S., Watson, Z. T., Graham, J. P., & Kim, K. Y. (2014). Fault-controlled CO_2 leakage from natural reservoirs in the colorado plateau, east-central Utah. *Earth*

and Planetary Science Letters, 403, 358–367. https://doi.org/10.1016/j.epsl.2014.07.012
Kämpf, H., Bräuer, K., Schumann, J., Hahne, K., & Strauch, G. (2013). CO_2 discharge in an active, non-volcanic continental rift region (czech republic): Characterisation ($\delta^{13}C$, $^3He/^4He$) and quantification of diffuse and vent CO_2 emissions. *Chemical Geology, 339*, 71–83. https://doi.org/10.1016/j.chemgeo.2012.08.005
Kulongoski, J. T., Hilton, D. R., Barry, P. H., Esser, B. K., Hillegonds, D., & Belitz, K. (2013). Volatile fluxes through the Big bend section of the san Andreas fault, California: Helium and carbon-dioxide systematics. *Chemical Geology, 339*, 92–102. https://doi.org/10.1016/10.1016/j.chemgeo.2012.09.007
Lehmann, B. E., Lehmann, M., Neftel, A., & Tarakanov, S. V. (2000). Radon-222 monitoring of soil diffusivity. *Geophysical Research Letter, 27*(23), 3917–3920. https://doi.org/10.1029/1999gl008469
Lewicki, J. L., Hilley, G. E., Dobeck, L., Mcling, T. L., Kennedy, B. M., Bill, M., & Marino, B. D. V. (2013). Geologic CO_2 input into groundwater and the atmosphere, soda springs, ID, USA. *Chemical Geology, 339*, 61–70. https://doi.org/10.1016/j.chemgeo.2012.06.013
Li, H., Xu, Z., Niu, Y., Kong, G., Huang, Y., Wang, H., Si, J., Sun, Z., Pei, J., Gong, Z., Chevalier, M. L., & Liu, D. (2014). Structural and physical property characterization in the Wenchuan earthquake Fault Scientific Drilling project - hole 1 (WFSD-1). *Tectonophysics, 619–620*, 86–100. https://doi.org/10.1016/j.tecto.2013.08.022
Li, J., Zhou, X. C., Shi, H. Y., Sun, F. X., Lu, L. N., Chen, C., Zeng, L. H., & Chen, Z. (2018). Environmental impact of CO_2, Rn and Hg emissions from the main faults of northwest region of the Beijing region, China. *Environmental Chemistry, 37*(5), 931–941. (in Chinese with English abstract).
Li, R., & Li, Y. (2008). Tectonic evolution of the western margin of the ordos basin (Central China). *Russian Geology and Geophysics, 49*(1), 1–27. https://doi.org/10.1016/j.rgg.2007.12.002
Li, Y., Du, J., Wang, X., Zhou, X., Xie, C., & Cui, Y. (2013). Spatial variations of soil gas geochemistry in the Tangshan area of Northern China. *Terrestrial, Atmospheric and Oceanic Sciences, 24*(3), 323–332. https://doi.org/10.3319/tao.2012.11.26.01(tt)
Lindqvist, O., Johansson, K., Aastrup, M., Andersson, A., Bringmark, L., Hovsenius, G., Håkansson, L., Iverfeldt, Å., Meili, M., & Timm, B. (1991). Mercury in the Swedish environment - Recent research on causes, consequences and corrective methods. *Water, Air, and Soil Pollution, 55*, 1–261. https://doi.org/10.1007/BF00542429
Liu, Z. F. (2020). Soil gas geochemistry characteristics in the western margin of the Ordos block, China. *Institute of Earthquake Forecasting, China Earthquake Administration*, 1–76 (in Chinese with English abstract).
Liu, J., Xie, F., & Lv, Y. (2016). Seismic hazard assessments for the ordos block and its periphery in China. *Soil Dynamics and Earthquake Engineering, 84*(1), 70–82. https://doi.org/10.1016/j.soildyn.2016.02.007
Liu, Z. F., Li, Y., Chen, Z., Cui, Y. J., Lu, C., Yang, J., & Zhao, Y. X. (2019). Gas emission from active fault zones around the Jilantai faulted depression basin and its implications for fault activities. *Acta Seismologica Sinica, 41*(5), 613–632. (in Chinese with English abstract).
Lombardi, S., & Voltattorni, N. (2010). Rn, He and CO_2 soil gas geochemistry for the study of active and inactive faults. *Applied Geochemistry, 25*(8), 2803–2815. https://doi.org/10.1016/j.apgeochem.2010.05.006
Lubin, J. H., Wang, Z. Y., Boice, J. D., Jr., Xu, Z. Y., Blot, W. J., De Wang, L., & Kleinerman, R. A. (2004). Risk of lung cancer and residential radon in China: Pooled results of two studies. *International Journal of Cancer, 109*(1), 132–137. https://doi.org/10.1002/ijc.11683
Martinelli, G. (2020). Previous, current, and future trends in research into earthquake precursors in geofluids. *Geosciences, 10*(189), 1–21. https://doi.org/10.3390/geosciences10050189
Martinelli, G., & Plescia, P. (2003). Carbon dioxide and methane emissions from calcareous-marly rock under stress: Experimental tests results. *Annals of Geophysics, 48*, 167–173. https://doi.org/10.4401/ag-3191
Muller, G. (1969). Index of geoaccumulation in sediments of the Rhine River. *Geological Journal, 2*(3), 108–118.
Papp, B., Deák, F., Horváth, Á., Kiss, Á., Rajnai, G., & Szabó, C. (2008). A new method for the determination of geophysical parameters by radon concentration measurements in bore-hole. *Journal of Environmental Radioactivity, 99*(11), 1731–1735. https://doi.org/10.1016/j.jenvrad.2008.05.005
Park, S., Bae, J., Nam, B. H., & Yoo, K. Y. (2008). Aetiology of cancer in Asia. *Asian Pacific Journal of Cancer Prevention, 9*(3), 371–380.
Pfanz, H., Yüce, G., Gulbay, A. H., & Gokgoz, A. (2019). Deadly CO_2 gases in the Plutonium of Hierapolis (Denizli, Turkey). *Archaeological and Anthropological Sciences, 11*(4), 1359–1371. https://doi.org/10.1007/s12520-018-0599-5
Phuong, N. K., Harijoko, A., Itoi, R., & Unoki, Y. (2012). Water geochemistry and soil gas survey at Ungaran geothermal field, central Java, Indonesia. *Journal of Volcanology and Geothermal Research, 229*, 23–33. https://doi.org/10.1016/j.jvolgeores.2012.04.004
Pirrone, N., Cinnirella, S., Feng, X., Finkelman, R. B., Friedli, H., Leaner, J., Mason, R., Mukherjee, A. B., Stracher, G. B., Streets, D. G., & Telmer, K. (2010). Global mercury emissions to the atmosphere from anthropogenic and natural sources. *Atmospheric Chemistry and Physics, 10*, 5951–5964. https://doi.org/10.5194/acp-10-5951-2010
Ring, U., Uysal, I. T., Yüce, G., Ünal-İmer, E., Italiano, F., Imer, A., & Zhao, J. (2016). Recent mantle degassing recorded by carbonic spring deposits along sinistral strike-slip faults, south-central Australia. *Earth and Planetary Science Letters, 454*, 304–318. https://doi.org/10.1016/j.epsl.2016.09.017
Rizzo, A. L., Uysal, I. T., Mutlu, M., Unal-Imer, E., Dirik, K., Yüce, G., Caracausi, A., Italiano, F., Misseri, M., Temel, A., Bayari, S., Özyurt, N., & Zhao, J. (2019). Geochemistry of fluid inclusions in travertines from Western and Northern Turkey: Inferences on the role of active faults in fluids circulation. *Geochemistry, Geophysics, Geosystems, 20*(11), 5473–5498. https://doi.org/10.1029/2019GC008453

Tao, M. X., Xu, Y. C., Shi, B. G., Jiang, Z. T., Shen, P., Li, X. B., & Sun, M. L. (2005). Characteristics of mantle degassing and deep-seated geological structures in different typical fault zones of China. *Science in China, Series D: Earth Sciences, 48*(7), 1074–1088.

Tennant, R., Johnston, H. J., & Wells, J. B. (1961). Acute bilateral pneumonitis associated with the inhalation of mercury vapor-report of 5 cases. *Connecticut Medicine, 25*, 106–109.

The Research Group on "Active Fault System around Ordos Massif", State Seismological Bureau (SSB). (1988). Active fault system around Ordos massif. *Seismological Press, Beijing*, 1–335 (in Chinese).

Toutain, J. P., & Baubron, J. C. (1999). Gas geochemistry and seismotectonics: A review. *Tectonophysics, 304*(1), 1–27. https://doi.org/10.1016/S0040-1951(98)00295-9

Varley, N. R., & Flowers, A. G. (1993). Radon in soil gas and its relationship with some major faults of SW England. *Environmental Geochemistry and Health, 15*(2–3), 145–151. https://doi.org/10.1007/bf02627832

Walia, V., Yang, T. F., Hong, W. L., Lin, S. J., Fu, C. C., Wen, K. L., & Chen, C. H. (2009). Geochemical variation of soil-gas composition for fault trace and earthquake precursory studies along the Hsincheng fault in NW Taiwan. *Applied Radiation and Isotopes, 67*, 1855–1863. https://doi.org/10.1016/j.apradiso.2009.07.004

Wang, X., Li, Y., Du, J., & Zhou, X. (2014). Correlations between radon in soil gas and the activity of seismogenic faults in Tangshan area, North China. *Radiation Measurements, 60*, 8–14. https://doi.org/10.1016/j.radmeas.2013.11.001

Wang, Y., Wang, M., & Shen, Z. K. (2017). Block-like versus distributed crustal deformation around the northeastern Tibetan plateau. *Journal of Asian Earth Sciences, 140*, 31–47. https://doi.org/10.1016/j.jseaes.2017.02.040

Wang, Y., Zhang, S., & Yuce, G. (2018). Gas geochemistry: From conventional to unconventional domains. *Marine and Petroleum Geology, 89*(1), 1–3. https://doi.org/10.1016/j.marpetgeo.2017.08.023

Wei, Y., & Wang, Y. (2004). Comparison of enrichment patterns of various energy resources in ordos basin. *Oil and Gas Geology, 25*(4), 385–392. (in Chinese with English abstract).

Wesnousky, S. G., Jones, L. M., Scholz, C. H., & Deng, Q. (1984). Historical seismicity and rates of crustal deformation along the margins of the Ordos block, north China. *Bulletin of the Seismological Society of America, 74*(5), 1767–1783.

Winkler, R., Ruckerbauer, F., & Bunzl, K. (2001). Radon concentration in soil gas: A comparison of the variability resulting from different methods, spatial heterogeneity and seasonal fluctuations. *Science of the Total Environment, 272*(1), 273–282. https://doi.org/10.1016/s0048-9697(01)00704-5

Yang, Y., Li, Y., Guan, Z. J., Chen, Z., Zhang, L., Lv, C. J., & Sun, F. X. (2018). Correlations between the radon concentrations in soil gas and the activity of the Anninghe and the Zemuhe faults in Sichuan, southwestern of China. *Applied Geochemistry, 89*, 23–33. https://doi.org/10.1016/j.apgeochem.2017.11.006

Yıldırım, G., Mutlu, H., Karabacak, V., Uysal, I. T., Dirik, K., Temel, A., Yüce, G., & Zhao, J. X. (2020). Temporal changes in geochemical-isotopic systematics of the late Pleistocene Akkaya travertines (Turkey) - Implications for fluid flow circulation and seismicity. *Geochemistry, 80*(4), 1–16. https://doi.org/10.1016/j.chemer.2020.125630

Yin, A., & Harrison, T. M. (2000). Geologic evolution of the Himalayan-Tibetan orogen. *Annual Review of Earth and Planetary Sciences, 28*, 211–280. https://doi.org/10.1146/annurev.earth.28.1.211

Yuce, G., Fu, C. C., D'Alessandro, W., Gulbay, A. H., Lai, C. W., Bellomo, S., Yang, T. F., Italiano, F., & Walia, V. (2017). Geochemical characteristics of soil radon and carbon dioxide within the dead sea fault and Karasu fault in the Amik basin (Hatay), Turkey. *Chemical Geology, 469*, 129–146. https://doi.org/10.1016/j.chemgeo.2017.01.003

Yuce, G., & Gasparon, M. (2013). Preliminary Risk Assessment of Radon in Groundwater: A case study from Eskisehir. *Turkey Isotopes in Environmental and Health Studies, 49*(2), 163–179. https://doi.org/10.1080/10256016.2013.739562

Yuce, G., Italiano, F., D'Alessandro, W., Yalcin, T. H., Yasin, D. U., Gulbay, A. H., Ozyurt, N. N., Rojay, B., Karabacak, V., Bellomo, S., Brusca, L., Yang, T., Fu, C. C., Lai, C. W., Ozacar, A., & Walia, V. (2014). Origin and interactions of fluids circulating over the Amik Basin (Hatay-Turkey) and relationships with the hydrologic, geologic and tectonic settings. *Chemical Geology, 388*, 23–39. https://doi.org/10.1016/j.chemgeo.2014.09.006

Yuce, G., Ugurluoglu, Y. D., Nadar, N., Yalcin, H. T., Yaltirak, C., Streil, T., & Oeser, V. (2010). Monitoring of earthquake precursors by multi-parameter stations in Eskisehir Region (Turkey). *Applied Geochemistry, 25*(4), 572–579. https://doi.org/10.1016/j.apgeochem.2010.01.013

Zhan, Y., Zhao, G., Wang, J., Tang, J., Chen, X., Deng, Q., Xuan, F., & Zhao, J. (2005). Crustal electric structure of Haiyuan arcuate tectonic region in the northeastern margin of Qinghai-Xizang plateau, China. *Acta Seismologica Sinica, 27*(4), 431–440. (in Chinese with English abstract).

Zhang, Y. Q., Shi, W., & Dong, S. (2011). Changes of late Mesozoic tectonic regimes around the Ordos Basin (north China) and their geodynamic implications. *Acta Geologica Sinica, 85*(6), 1254–1276. (in Chinese with English abstract).

Zheng, G., Ma, X., Guo, Z., Hilton, D. R., Xu, W., Liang, S., Fan, Q., & Chen, W. (2017). Gas geochemistry and methane emission from Dushanzi mud volcanoes in the southern Junggar Basin, NW China. *Journal of Asian Earth Sciences, 149*, 184–190. https://doi.org/10.1016/j.jseaes.2017.08.023

Zheng, G., Xu, S., Liang, S., Shi, P., & Zhao, J. (2013). Gas emission from the Qingzhu river after the 2008 Wenchuan Earthquake, Southwest China. *Chemical Geology, 339*, 187–193. https://doi.org/10.1016/j.chemgeo.2012.10.032

Zhou, X., Chen, Z., & Cui, Y. (2016). Environmental impact of CO2, Rn, Hg degassing from the rupture zones produced by Wenchuan MS 8.0 earthquake in western Sichuan. China. *Environmental Geochemistry and Health, 38*(5), 1067–1082. https://doi.org/10.1007/s10653-015-9773-1

Zhou, X., Du, J., Chen, Z., Cheng, J., Tang, Y., Yang, L., Xie, C., Cui, Y., Liu, L., Yi, L., Yang, P., & Li, Y. (2010). Geochemistry of soil gas in the seismic fault zone produced by the Wenchuan MS 8.0 earthquake, southwestern China. *Geochemical Transactions, 11*(5), 1–10. https://doi.org/10.1186/1467-4866-11-5

Zhou, X. C., Sun, F. X., Chen, Z., Lü, C. J., Li, J., Wu, K. T., & Du, J. G. (2017). Degassing of CO2, CH4, Rn and Hg in the rupture zones produced by Wenchuan MS 8.0 earthquake. *Acta Petrologica Sinica, 33*(1), 291–303. (in Chinese with English abstract).